

Identification of anisoelectricity for electrostatic “trimming” of rate integrating gyroscopes

Chris C. Painter and Andrei M. Shkel

Microsystems Laboratory, Department of Mechanical and Aerospace Engineering
University of California, Irvine, CA, USA

ABSTRACT

This paper describes a technique for detection of anisoelectricities in rate integrating gyroscopes as part of a self-calibrative control architecture. In contrast to laser trimming typically done in post processing to compensate for structural imperfections, the on-chip control architecture uses feedforward voltage control to tune the nonlinear negative spring effects inherent in parallel plate electrodes in order to electrostatically “trim” the structural non-idealities. As the first steps toward the feedforward control realization, we present three different algorithms that can be implemented on-chip for identification of structural anisoelectricities. The first technique utilizes the results of measured static deflections, requiring precise knowledge of the displacements and applied forces. The second technique involves solving for the non-ideal stiffness parameters using Principal Component Analysis and Fourier transforms of the dynamic system response. The last technique embellishes on the second by the addition of an energy compensation control to overcome damping effects in low Q systems. Finally, the implementation of this algorithm in the electrostatic “trimming” of structural imperfections is discussed.

Keywords: Anisoelectricity, Rate Integrating Gyroscopes, Feedforward Control, Smart MEMS, Electrostatic Trimming

1. INTRODUCTION

With the successful application of solid-state sensors in the market, there is a high demand for devices with increased durability, precision, and robustness. In its current maturity, fabrication technologies fall below the tolerancing required for high precision devices, requiring active feedback control or post processing such as laser trimming to achieve design goals. This demand gives rise to devices with enhanced capabilities, such as structural compensation, integration of signal processing, and self-calibration functionality. To operate with the highest precision, vibratory rate gyroscopes^{1,2} typically include on-board electronics implementing a feedback control strategy to compensate for structural anisoelectricities that are a consequence of fabrication imperfections. This strategy suffices as long as the perturbation forces caused by the imperfections are comparable to the Coriolis force. However, preliminary observations on a prototype rate integrating gyroscope⁵ show large frequency mismatches and coupling due to fabrication imperfections (Figure 1). When imperfections are large compared to the Coriolis force, compensation cannot be achieved with a purely feedback control without influencing the Coriolis measurements. For example, in angle sensing gyroscopes, feedback forces on the order of the Coriolis force tend to disrupt the precession used to detect the angular position.

An alternative to a purely feedback control architecture is to implement a “smart” MEMS gyroscope⁴ with self-calibration capabilities that enable the device to identify its own system characteristics such as stiffness and damping utilizing an on-chip self-test algorithm. A “smart” MEMS gyroscope of this type would be able to identify large structural imperfections due to manufacturing variations and compensate for them with a feedforward type of control architecture (Figure 2) (i.e. electronic “trimming”). The feedforward control works in unison with a feedback control used to compensate for small perturbations that may arise during the normal operation of the device. This paper discusses several strategies for determining large anisoelectricities in order to design the feedforward portion of the two-stage control architecture.

The first part of this paper presents the ideal and non-ideal dynamics of a studied rate integrating gyroscope, showing the effects of implementing a purely feedback control. The second part of this paper discusses the

Further author information: (Send correspondence to C.C.P.)

C.C.P.: E-mail: cpainter@uci.edu, Telephone: (949) 824-6314, Address: 4200 Engineering Gateway; Irvine, CA 92697

A.M.S.: E-mail: ashkel@uci.edu, Telephone: (949) 824-3843

Web: <http://mems.eng.uci.edu>

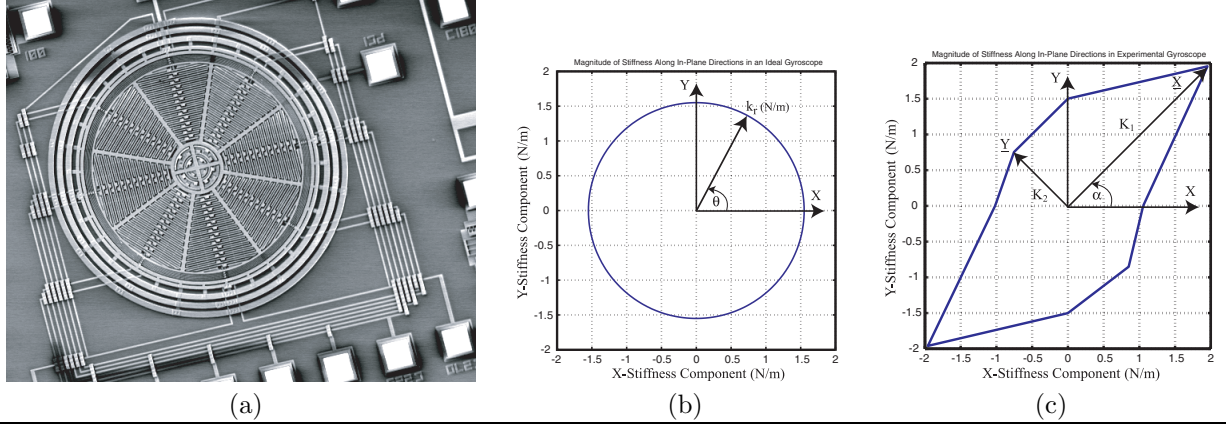


Figure 1. (a) A prototype surface machined rate integrating gyroscope was fabricated using JDS Uniphase’s MUMPS process. (b) In an ideal gyroscope, the stiffness would be identical along any arbitrary direction ($k_r(\theta) = \text{constant}$). (c) In the prototype gyroscope, the stiffness along the two drive axes and two sense axes is estimated by observing the natural frequency along each direction and knowing the ideal mass of the system. The plot of stiffness magnitude along the four directions shows large frequency mismatches ($K_1 - K_2 = 1.6$) and coupling (rotation of the stiffness axes by angle $\alpha = 45^\circ$).

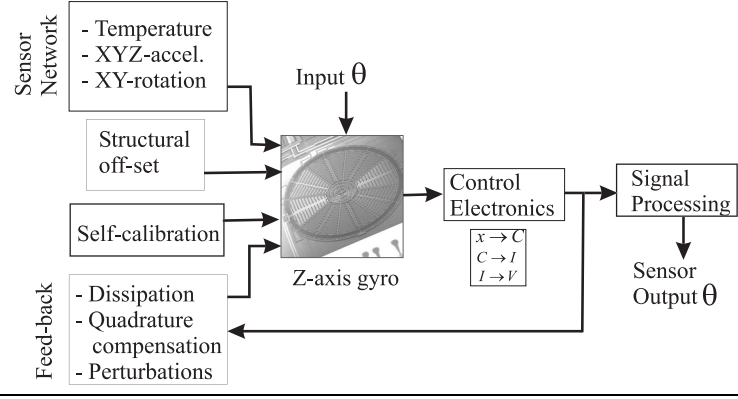


Figure 2. A Smart MEMS device would be capable of using the results of self-calibration for large error compensation using a feedforward and structural off-set type of control architecture. A feedback control would work in tandem to compensate for small perturbations arising during operation of the device.

fundamentals of three algorithms proposed for identifying the structural anisoeasticities in the system. The algorithm suite consists of a static deflection algorithm, a dynamic measurement algorithm, and a dynamic measurement with energy compensation algorithm. The third part of the paper presents the results of numerical simulation utilizing each of the three algorithms. Finally, we discuss implementation of the algorithm results in a feedforward control consisting of electrostatic tuning using parallel plate electrodes.

2. GYROSCOPE DYNAMICS AND FEEDBACK CONTROL

The studied gyroscope³ consists of a two degree of freedom lumped mass-spring system which uses electrostatic parallel plates for drive and sense (Figure 3a). The six interconnected ring suspension around the perimeter of the device provides necessary stiffness isotropy required for the successful operation of the device.⁵ The lumped mass-spring dynamics of this system are expressed by⁶

$$\begin{aligned} \ddot{x} + \omega_n^2 x - 2m\Omega\dot{y} &= 0 \\ \ddot{y} + \omega_n^2 y + 2m\Omega\dot{x} &= 0 \end{aligned} \quad (1)$$

where ω_n is the natural frequency, Ω is the input angular velocity, and we are assuming that the system is initially freely vibrating. Over time, the line of oscillation will precess by an angle ϕ (Figure 3b), which can be

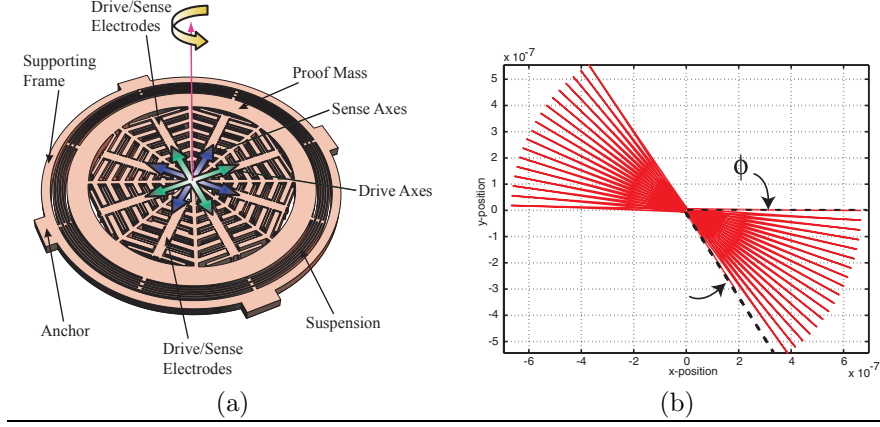


Figure 3. (a) The studied rate integrating gyroscope³ consists of a freely vibrating proof mass attached to a concentric six ring suspension. Stationary electrodes interwoven throughout the mass along the drive axes help sustain motion while electrodes along the sense axes sense deflection and velocity used to calculate the Coriolis induced deflection angle. (b) In ideal operation, Coriolis force causes the line of oscillation initially aligned with the horizontal axis attached to the rotating frame to precess by an angle ϕ .

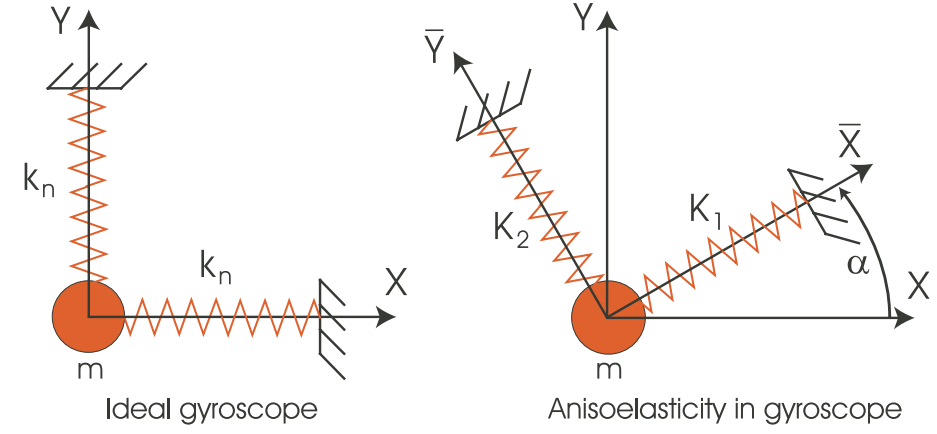


Figure 4. In the ideal gyroscope, the principal axes of elasticity have equal stiffness and coincide with the x-y coordinate system. In the presence of imperfections, there is a mismatch in the principal stiffness values, $2h = (K_1 - K_2)$ and an angular mismatch of the principal axes from the x-y coordinate system by an angle α .

calculated by

$$\tan \phi = \frac{2(\omega_n^2 xy + \dot{x}\dot{y})}{\omega_n^2(x^2 - y^2) + (\dot{x}^2 - \dot{y}^2)} \quad (2)$$

However, anisoelectricities due to fabrication imperfections disrupt isotropy of the suspension, causing frequency mismatch and mode coupling. The non-ideal dynamics of the gyroscope, assuming no damping, can then be expressed by

$$\begin{aligned} m\ddot{x} + k_{xx}x + k_{xy}y - 2\Omega\dot{y} &= F_x \\ m\ddot{y} + k_{yy}y + k_{yx}x + 2\Omega\dot{x} &= F_y \end{aligned} \quad (3)$$

where m is the lumped mass approximation for the gyroscope, k_{xx} , k_{yy} , k_{xy} , and k_{yx} are the non-ideal stiffness terms, and F_x and F_y are applied forces. The non-ideal stiffness terms can also be expressed in terms of the principal stiffness values, K_1 and K_2 , and the angular mismatch angle, α , of the principal axes of elasticity with the x-y coordinate system (Figure 4)⁷

$$\begin{aligned} k_{xx} &= \frac{K_1 + K_2}{2} + \frac{K_1 - K_2}{2} \cos(2\alpha) \\ k_{yy} &= \frac{K_1 + K_2}{2} - \frac{K_1 - K_2}{2} \cos(2\alpha) \end{aligned} \quad (4)$$

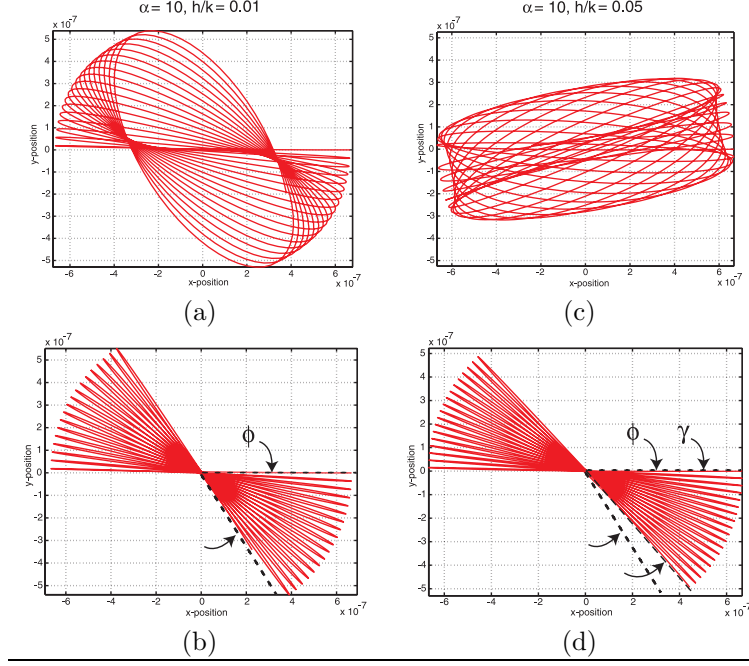


Figure 5. (a) Anisoelasticities result in quadrature error which manifests as a developing elliptical pattern during precession of the straight line of oscillation. (b) With the use of feedback control, these imperfections can be compensated for while preserving the angle of precession ϕ . Here the angle of misalignment is 10 degrees and the principal axes stiffness mismatch is 1% of the ideal isotropic stiffness (c) Larger errors result in more erratic oscillation patterns, but can still be compensated for using the same feedback control. (d) However, the feedback control disrupts the line of oscillation, reducing the precession angle from the ideal angle ϕ to γ . Here the angle of misalignment is 10 degrees and the principal axis stiffness mismatch is 5% of the ideal isotropic stiffness

$$k_{xy} = k_{yx} = \frac{K_1 - K_2}{2} \sin(2\alpha)$$

In the ideal gyroscope, it is necessary for the stiffness along the principal axes, and thus along any arbitrary axis, to be identical. Then we can express Equation (4) as perturbations from an ideal isotropic stiffness k_n

$$\begin{aligned} k_{xx} &= k_n + h \cos(2\alpha) \\ k_{yy} &= k_n - h \cos(2\alpha) \\ k_{xy} &= k_{yx} = h \sin(2\alpha) \end{aligned} \quad (5)$$

where $2k_n = (K_1 + K_2)$ and h is proportional to the stiffness mismatch between the principal axes, $2h = (K_1 - K_2)$. An appropriate feedback control which will compensate for anisoelasticity while not interfering with the Coriolis force is of the form⁶

$$\begin{Bmatrix} F_x \\ F_y \end{Bmatrix} = -\gamma_1 \cdot P \cdot S^T \cdot \begin{Bmatrix} x \\ y \end{Bmatrix} \quad (6)$$

where γ_1 is a constant gain, S is a 2×2 skew symmetric matrix, and P is quadrature defined as

$$P = \pi(\dot{x}y - y\dot{x}) \quad (7)$$

The feedback controller is sufficient to compensate for imperfections while not interfering with the Coriolis force as long as the imperfections are sufficiently small (e.g. $\alpha = 10$ degrees and h is 1% of the ideal stiffness) (Figure 5a,b). However, typically the imperfections are large (see Figure 1, $\alpha = 45$ and $h = 50\%$ of the ideal stiffness) and while the controller will still compensate for the errors, it will interfere with the measured precession angle (Figure 5c,d). Therefore, it is necessary to implement a feedforward control to compensate for large anisoelasticities while retaining a feedback control to correct for small errors that develop during operation of the device.

3. ANISOELASTICITY ALGORITHMS

The first step in developing the feedforward control is to develop algorithms used to determine the structural imperfections in the system as part of a self-calibration diagnostic test. Here we present three different algorithms for obtaining the non-ideal stiffness parameters for the gyroscope. The relative merits of each algorithm are described.

3.1. Static Deflections

In the absence of rotation and assuming a constant input force and symmetric stiffness matrix ($k_{yx} = k_{xy}$), Equation (3) simplifies to the static equation

$$\begin{bmatrix} k_{xx} & k_{xy} \\ k_{xy} & k_{yy} \end{bmatrix} \begin{Bmatrix} x \\ y \end{Bmatrix} = \begin{Bmatrix} F_x \\ F_y \end{Bmatrix} \quad (8)$$

In the presence of the off-diagonal elements k_{xy} , a static force applied in one direction will result not only in deflection along the direction of applied force, but also a deflection component orthogonal to the applied force. By measuring the deflection in the direction of the applied force and the resulting orthogonal deflection, we can calculate both the on-diagonal and off-diagonal stiffness values.

We first apply a static force along the y axis ($F_x = 0, F_y = F$) and measure the deflection along both x (δ_1) and y (δ_2). Next, we apply the same static force along the x axis ($F_x = F, F_y = 0$) and again measure the x (δ_3) and y deflections (δ_4). Solving for the deflections in all three cases gives

$$\begin{aligned} \frac{\delta_1}{F} &= -\frac{k_{xy}}{k_{xx}k_{yy} - k_{xy}^2} & \frac{\delta_3}{F} &= \frac{k_{yy}}{k_{xx}k_{yy} - k_{xy}^2} \\ \frac{\delta_2}{F} &= \frac{k_{xx}}{k_{xx}k_{yy} - k_{xy}^2} & \frac{\delta_4}{F} &= -\frac{k_{xy}}{k_{xx}k_{yy} - k_{xy}^2} \end{aligned} \quad (9)$$

Noting that $\delta_1 = \delta_4$ because of symmetry of the stiffness matrix, we disregard the δ_4 equation which gives redundant information. With the remaining deflection equations, we solve for the elements of the stiffness matrix

$$\begin{aligned} k_{xx} &= \frac{F\delta_1}{\delta_1\delta_3 - \delta_2^2} \\ k_{yy} &= \frac{F\delta_3}{\delta_1\delta_3 - \delta_2^2} \\ k_{xy} &= \pm \frac{F\delta_2}{\delta_1\delta_3 - \delta_2^2} \end{aligned} \quad (10)$$

Here, the sign of the k_{xy} term is dependent on the mismatch and orientation of the principal axes of elasticity. In order to find the sign, it is necessary to first make an initial guess of k_{xy} and substitute this value back into the δ_2 deflection equation of Equation (10). If the sign of the right hand side matches the sign of the measured deflection, then the initial guess is correct. If the sign is different, then it is necessary to reverse the sign of the guessed k_{xy} value.

The advantages of using this kind of detection scheme is its inherent simplicity. The disadvantages of such a technique is that it is limited by the accuracy of measuring deflections and applying forces. Accurate sensing of the deflection is limited by the sense electronics in the form of thermal and electronic noise while accurate application of forces relies on good understanding of the nature of the applied force. This can be a difficult task in drive schemes utilizing nonlinear or position dependent forces, such as electrostatically driven parallel plate devices. The issues of precision detection of positions and forces can be solved by considering the dynamic response of the system and using techniques that take advantage of all the data through averaging. These techniques are discussed next.

3.2. Unforced Dynamic Detection

Substituting Equation(5) into Equation (3) and solving for x and y assuming no angular rotation ($\Omega = 0$), no damping, and an initial deflection of x_0 and y_0 yields

$$\begin{aligned} \begin{Bmatrix} x \\ y \end{Bmatrix} &= \begin{bmatrix} 1 + \cos 2\alpha & \sin 2\alpha \\ \sin 2\alpha & 1 - \cos 2\alpha \end{bmatrix} \begin{Bmatrix} x_0 \\ y_0 \end{Bmatrix} \cos \sqrt{\left(\omega_n^2 + \frac{h}{m}\right)t} + \\ &\quad \begin{bmatrix} 1 - \cos 2\alpha & -\sin 2\alpha \\ -\sin 2\alpha & 1 + \cos 2\alpha \end{bmatrix} \begin{Bmatrix} x_0 \\ y_0 \end{Bmatrix} \cos \sqrt{\left(\omega_n^2 - \frac{h}{m}\right)t} \end{aligned} \quad (11)$$

or in non-matrix form as

$$\begin{aligned} x(t) &= \frac{1}{2} (G(\alpha) + x_0) \cos \left(\sqrt{\left(\omega_n^2 + \frac{h}{m}\right)t} \right) - \frac{1}{2} (G(\alpha) - x_0) \cos \left(\sqrt{\left(\omega_n^2 - \frac{h}{m}\right)t} \right) \\ y(t) &= \frac{1}{2} (H(\alpha) + y_0) \cos \left(\sqrt{\left(\omega_n^2 + \frac{h}{m}\right)t} \right) - \frac{1}{2} (H(\alpha) - y_0) \cos \left(\sqrt{\left(\omega_n^2 - \frac{h}{m}\right)t} \right) \end{aligned} \quad (12)$$

$$\begin{aligned} G(\alpha) &= \sin(2\alpha) y_0 + \cos(2\alpha) x_0 \\ H(\alpha) &= -\cos(2\alpha) y_0 + \sin(2\alpha) x_0 \\ \omega_n^2 &= \frac{k_n}{m} \end{aligned}$$

We see that each position is comprised of the summation of two different sinusoidal functions due to the stiffness coupling. A plot of the time response of the system is a family of Lissajous figures (Figure 6). Over time, it can be seen that the Lissajous figures will have trajectories bounded by a rectangle whose size is defined by h and which is oriented at the angle α from the coordinate axis. To determine the orientation of the principal axes, we employ the statistical method of principal component analysis (PCA).

Here we will discuss the applications of PCA as it pertains to this study; a more general explanation can be found in.⁸ In our case, we have two variables of interest, the x position and y position. Now consider a 2×1 vector $\mathbf{V} = (x, y)$. We will assume that x and y have zero mean (centered about the origin) and that we have experimentally acquired covariances between x and y . A covariance matrix \mathbf{S} can be expressed by

$$\mathbf{S} = \begin{bmatrix} s_x^2 & s_{xy} \\ s_{xy} & s_y^2 \end{bmatrix} \quad (13)$$

where s_x^2 and s_y^2 are the variances of x and y and the covariance between x and y is

$$s_{xy} = \frac{n \sum_{k=1}^n x_k y_k - \sum_{k=1}^n x_k \sum_{k=1}^n y_k}{[n(n-1)]} \quad (14)$$

with the index of summation, k , going over the entire sample size, n . The covariance matrix is a numerical measure of the coupling between variables and in the case when \mathbf{S} is diagonal, the vectors of \mathbf{V} are uncorrelated, i.e. the x position has no influence on the y position. Notice, when there is coupling through the stiffness matrix between the x and y position, the covariance matrix will also have coupling. Thus, a transformation that diagonalizes the covariance matrix will also diagonalize the stiffness matrix. We now introduce a coordinate transformation $\zeta = \mathbf{U}^T \mathbf{V}$ where \mathbf{U} is a constant matrix of transformation. It can be shown that there exists such an orthogonal transformation \mathbf{U} such that the covariance matrix $\tilde{\mathbf{S}}$ of this new coordinate system is⁸

$$\tilde{\mathbf{S}} = E(\zeta \zeta^T) = \mathbf{U}^T \mathbf{S} \mathbf{U} \quad (15)$$

We will assume that the transformation \mathbf{U} is a unity gain rotation and so $\mathbf{U}^T = \mathbf{U}^{-1}$. With this assumption, we see that by choosing the columns of \mathbf{U} to be the eigenvectors (\mathbf{e}_1 and \mathbf{e}_2) of the covariance matrix, we will achieve a diagonal form, thus the eigenvectors designate the basis vectors for the uncoupled space. Since \mathbf{S} is Grammian, we are guaranteed of these eigenvectors being orthogonal. From Equation (5), we can see that a rotation transformation of the form

$$\begin{Bmatrix} x \\ y \end{Bmatrix} = \begin{bmatrix} \cos \alpha & -\sin \alpha \\ \sin \alpha & \cos \alpha \end{bmatrix} \begin{Bmatrix} q_1 \\ q_2 \end{Bmatrix} \quad (16)$$

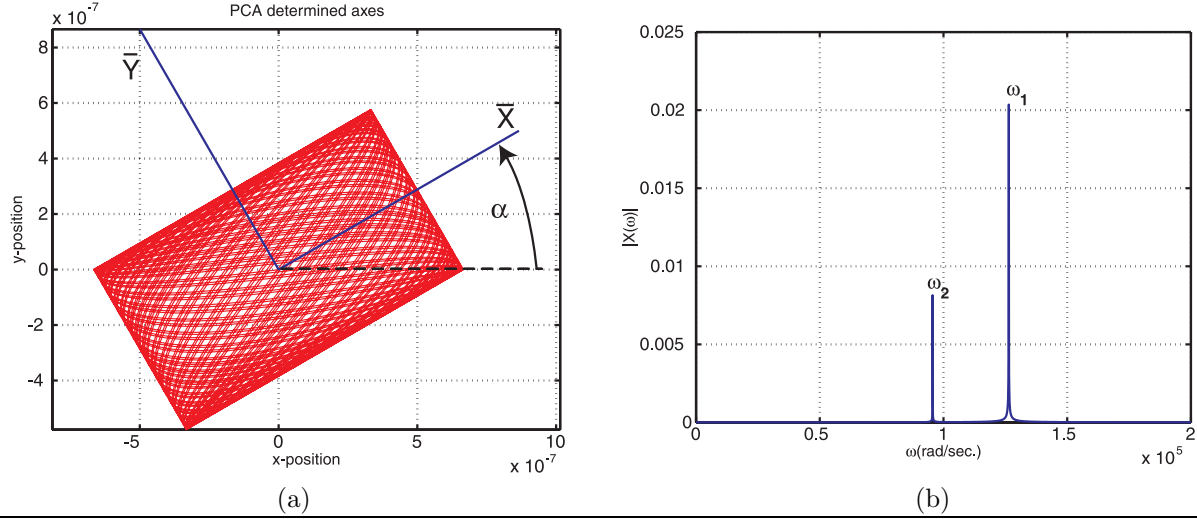


Figure 6. (a) In the absence of damping, the trajectory of the gyroscope will form into elliptical type Lissajous figures. These figures will be bound by a rectangle oriented at an angle α . A Principal Component Analysis (PCA) is used to determine the principal axes of elasticity, designated as \bar{X} and \bar{Y} . (b) The Fourier transform of the x component of the data reveals two peaks due to off diagonal coupling of the stiffness matrix. From this plot, the h parameter of the system can be extracted as $2h = m(\omega_1^2 - \omega_2^2)$ where ω_1 and ω_2 correspond to the frequencies of the maximum and second maximum peaks, respectively.

will uncouple the dynamic system to the uncorrelated principal axis coordinate system. It is necessary that this transformation must be equivalent to \mathbf{U}^T and so one expression for the eigenvectors representing the principal axes is (Figure 6a)

$$\begin{aligned} \mathbf{e}_1 &= (\cos \alpha) \hat{e}_x - (\sin \alpha) \hat{e}_y \\ \mathbf{e}_2 &= (\sin \alpha) \hat{e}_x + (\cos \alpha) \hat{e}_y \end{aligned} \quad (17)$$

We then directly calculate the angle α from the second eigenvector

$$\alpha = \tan^{-1} \left(\frac{e_{2,x}}{e_{2,y}} \right) \quad (18)$$

where $e_{2,x}$ and $e_{2,y}$ are the x and y components of the second eigenvector.

Based off the dynamic system in Equation (12), if we restrict the initial conditions to only an x deflection ($y_0 = 0$), then we are guaranteed of the system oscillating within a rectangle oriented in the boundary $\frac{\pi}{4} > \alpha > -\frac{\pi}{4}$. Taking a Fourier transform of Equation (12) while considering only the x position yields

$$\begin{aligned} X(\omega) &= \frac{1}{2} (G(\alpha) + x_0) \pi \delta(\omega - \omega_1) + \frac{1}{2} (G(\alpha) - x_0) \pi \delta(\omega - \omega_2) \\ \omega_1^2 &= \omega_n^2 + \frac{h}{m} \\ \omega_2^2 &= \omega_n^2 - \frac{h}{m} \end{aligned} \quad (19)$$

From Equation (19), assuming the initial y deflection is zero, the ratio of the amplitudes of the two frequency components are

$$\left| \frac{X(\omega_1)}{X(\omega_2)} \right| = x_0 \frac{\cos(2\alpha) + 1}{\cos(2\alpha) - 1} \quad (20)$$

In this case, the highest peak in the frequency plot corresponds to the ω_1 term and the second highest peak corresponds to ω_2 term (Figure 6b). Parameter h and the ideal isotropic stiffness k_n are calculated as $2h = m(\omega_1^2 - \omega_2^2)$ and $2k_n = m(\omega_1^2 + \omega_2^2)$, respectively. If $\omega_1 < \omega_2$, then $h < 0$.

The algorithm for determining h and k_n is dependent on differentiating the two peaks in the X frequency domain. As the errors tend to grow smaller, it becomes impossible to distinguish the two peaks and any numerical peak finding algorithm may result in erroneous results. A more accurate method for determining h and k_n requires the calculated α from the PCA analysis. Using the transformation from Equation (16), the equations in the transformed principal coordinate space are

$$\begin{aligned} q_1(t) &= (2x_0 \cos \alpha + 2y_0 \sin \alpha) \cos \left(\sqrt{\left(\omega_n^2 + \frac{h}{m}\right)t} \right) \\ q_2(t) &= (-2x_0 \sin \alpha + 2y_0 \cos \alpha) \cos \left(\sqrt{\left(\omega_n^2 - \frac{h}{m}\right)t} \right) \end{aligned} \quad (21)$$

Thus, if we transform our data in this way and then take the Fourier transform, we see that there will be one peak for q_1 and q_2 at frequencies ω_{q1} and ω_{q2} , respectively. These frequencies are

$$\begin{aligned} \omega_{q1}^2 &= \omega_n^2 + \frac{h}{m} \\ \omega_{q2}^2 &= \omega_n^2 - \frac{h}{m} \end{aligned} \quad (22)$$

Then, h and k_n are calculated simply as $2h = m(\omega_{q1}^2 - \omega_{q2}^2)$ and $2k_n = m(\omega_{q1}^2 + \omega_{q2}^2)$, respectively. This result makes it easier to identify smaller errors since it is only necessary to identify the largest peak in each frequency spectrum rather than the largest two.

The benefits of this algorithm is since the PCA and Fourier transforms take advantage of all the data, it is not necessary to have precise deflection information. This is especially advantageous in systems where small deflections are difficult to resolve due to noise in the sensing electronics. One of the shortcomings of this algorithm is that systems with high damping reduce the amount of data points, resulting in erroneous results. A solution to highly damped systems is vacuum packaging of the device and also to employ an energy compensating controller. The implementation of this controller is considered in the final part of this section.

3.2.1. Ambiguity of the algorithm

In our derivation of the angle α from Equation (17), we initially neglected the fact that the eigenvectors are interchangeable in the transformation matrix. Thus, another possible rotation angle is

$$\alpha_2 = \cot^{-1} \left(\frac{-e_{1,x}}{e_{1,y}} \right) \quad (23)$$

where α_2 is the angle calculated if we were to use the first eigenvector rather than the second. Here α_2 is related to the α calculated from Equation (18) by $\alpha_2 = \alpha - \text{sign}\{\alpha\} \left(\frac{\pi}{2}\right)$. Since the output from the PCA analysis is numerical values for the eigenvectors, it is impossible to tell \mathbf{e}_1 and \mathbf{e}_2 apart, thus the output PCA angle is either α or $\alpha - \text{sign}\{\alpha\} \left(\frac{\pi}{2}\right)$. However, we will show that even with this ambiguity in the angle, we will still arrive at an equivalent solution.

From Equation (19), if we make the substitution $\alpha = \alpha - \text{sign}\{\alpha\} \left(\frac{\pi}{2}\right)$, then the equation becomes

$$\left| \frac{X(\omega_1)}{X(\omega_2)} \right| = x_0 \frac{\cos(2\alpha) - 1}{\cos(2\alpha) + 1} \quad (24)$$

We see that the conditions are changed and now ω_2 corresponds to the first maximum peak and ω_1 corresponds to the second maximum peak. Now the algorithm will calculate $-h$ rather than h . If we substitute the two angle and h combinations of (α, h) and $(\alpha - \text{sign}\{\alpha\} \left(\frac{\pi}{2}\right), -h)$ into Equation (5), we will arrive at equivalent solutions. Thus, as long as the guess for α is between $-\frac{\pi}{4}$ and $\frac{\pi}{4}$, the algorithm will correctly identify the structural non-idealities whether the initial guess for α was correct or if it was actually $\alpha - \text{sign}\{\alpha\} \left(\frac{\pi}{2}\right)$.

3.3. Forced Dynamic Detection

In the previous section we were assuming no damping, letting the system to run indefinitely, allowing for an infinite amount of data. In reality, viscous damping will eventually deplete the energy of the system, resulting in a finite number of cycles from which to obtain data. In relatively high Q systems ($Q > 100$), there is sufficient energy to obtain enough data before the oscillation pattern dies out. However, in cases of low Q ($Q < 100$), there are not enough cycles to obtain an accurate calculation of the anisoeleasticities. For example, such Q

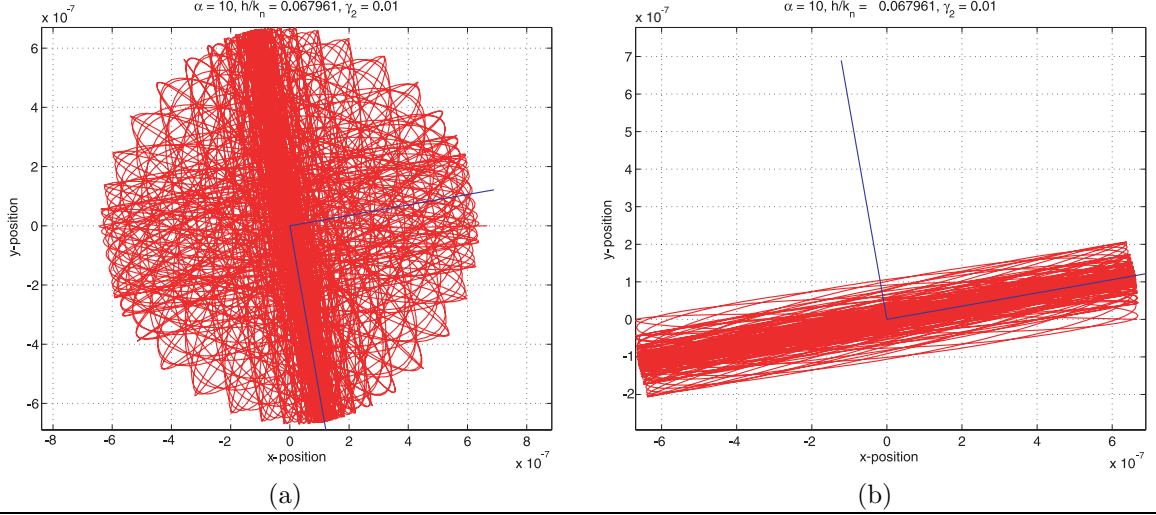


Figure 7. With the implementation of an energy compensating controller, the systems tends towards the principal axis with the lowest stiffness. In both these cases, α is the same, but the mismatch in the principal axis stiffness values is different: (a) $h > 0$ (b) $h < 0$

values are indicative of operating microstructures in an ambient atmosphere.⁹ In these cases, a controller to compensate for energy losses is required. In the angular gyroscope, a controller of the form⁶

$$\begin{Bmatrix} F_x \\ F_y \end{Bmatrix} = -\gamma_2 \cdot \Delta E \cdot \begin{Bmatrix} \dot{x} \\ \dot{y} \end{Bmatrix} \quad (25)$$

is implemented into Equation (3) that guarantees to maintain the energy of the system without interfering with the identification of anisoeleasticities. Here, γ_2 is a constant gain, \dot{x} and \dot{y} are the velocities along the x and y directions, and ΔE is the change in system energy given as

$$\Delta E = E_0 - \frac{\omega_n^2 (x^2 + y^2) + (\dot{x}^2 + \dot{y}^2)}{2} \quad (26)$$

where E_0 denotes nominal energy of the system normalized with respect to the effective mass. In using the controller, we have assumed isotropic damping with no coupling. This controller is based on small parameter variations¹⁰ and in order for the controller not to interfere with the measured parameters, the gain (γ_2) must be sufficiently small.

With the implementation of this controller, the oscillation of the system tends to propagate towards the principal axis with the smallest stiffness (Figure 7). We will assume that this is the \bar{x} axis (see Figure 4), which is misaligned from the x-axis by the angle α and is guaranteed of being oriented in the range of $-\frac{\pi}{2} < \alpha < \frac{\pi}{2}$. Now, we consider the dynamics in the transformed principal axis coordinate system from Equation (21). Taking the Fourier transform of q_1 and q_2 yields one peak for each at frequencies ω_{q1} and ω_{q2} respectively. From Equation (22), h is given as $2h = m(\omega_{q1}^2 - \omega_{q2}^2)$ and k_n is calculated by $2k_n = m(\omega_{q1}^2 + \omega_{q2}^2)$. The difference between this and the algorithm of the previous section is that we are assuming that q_1 is always the axis with the smallest stiffness. Thus, ω_{q1}^2 is always less than ω_{q2}^2 , so h is limited to being always less than zero. However, with the new limits of α from $-\frac{\pi}{2}$ and $\frac{\pi}{2}$, we have compensated for this restriction on h and the algorithms will still correctly calculate the stiffness non-idealities when substituting into Equation (5).

The advantages of this methodology are the same as the previous algorithm with the addition of energy compensation. As a result, systems with low Q can still be analyzed to determine the structural anisoeleasticities. In addition, no initial deflection is required and the controller will tend to drive the system to a pre-determined energy level. The caveat to this method is that the chosen gain of the energy compensation controller must be sufficiently small to avoid interfering with the measurement of the anisoeleasticity.

4. NUMERICAL SIMULATION

All simulation parameters are based off a realistic implementation of a surface micromachined rate integrating gyroscope (Figure 1). The mass used is 4.10×10^{-10} kg and the isotropic stiffness k_n is 1.55 N/m, giving a

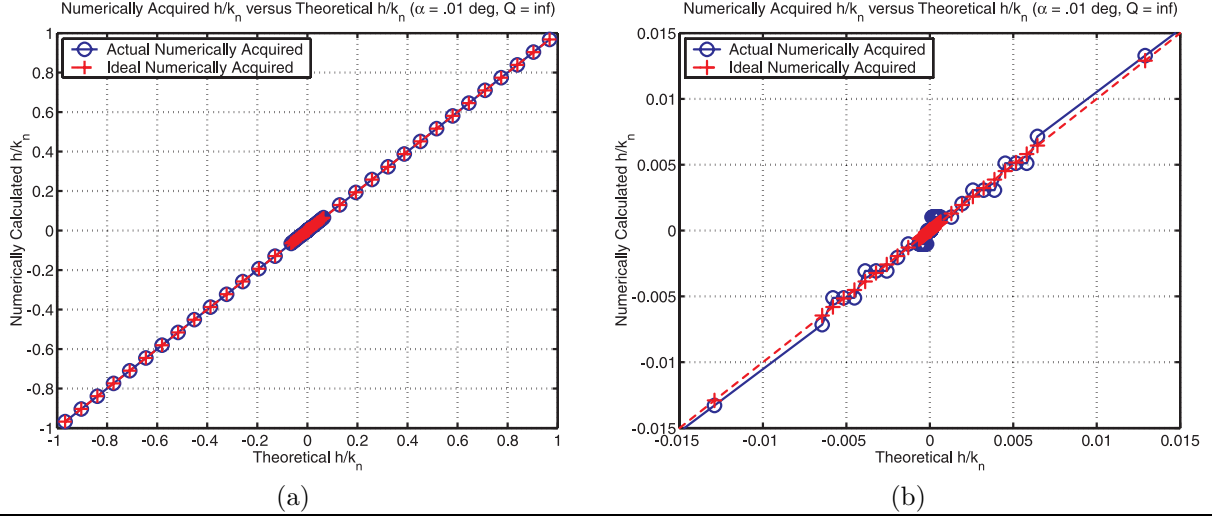


Figure 8. (a) In the case of the unforced dynamic detection, the algorithm can detect errors with a precision of .001 (the numerically acquired h/k_n = the theoretical $h/k_n \pm .001$) over the range of the theoretical h , making it suitable to detect anisoelectricity ranging from $100\% > |h/k_n| > 10\%$ with over 99% accuracy and $10\% > |h/k_n| > 1\%$ with over 90% accuracy. (b) As $|h/k_n|$ continues to decrease, the accuracy of the algorithm also continues to diminish. A fundamental lower limit is reached when $|h/k_n| = .1\%$ where the algorithm can no longer accurately detect errors.

natural frequency of 9.8 kHz for the system.

4.1. Static Deflection

This simulation is done using MATLAB where a known force of $1 \mu\text{N}$ is applied sequentially in the y direction and then in the x direction with the x and y deflections being measured in both cases. In the gyroscope, this applied force corresponds to a DC drive voltage of 13.8V, with a drive and sense capacitance of .021 pF. The Q is assumed to be 1000 in order to obtain a stable static deflection. Prior to running the simulation, errors are introduced into the stiffness matrix using the formulation from Equation (5) and then the simulation is run multiple times while varying α and h . Numerically, the algorithm can calculate stiffness non-idealities as small as .001% of the ideal stiffness.

4.2. Unforced Dynamic Deflection

The same MATLAB simulation is run, this time assuming an initial x deflection and no applied force. Using deflection data acquired from the dynamic system response, the eigenvectors corresponding to the principal axes orientation are determined using the MATLAB's PCA toolbox, which are then used to calculate the angle α . Parameter α is then used to transform the data into the principal coordinate frame and a Fourier transform of the principal coordinate deflections is obtained. A peak finding algorithm is then used to determine the frequencies of the two peaks and h and k_n are calculated based off the frequency difference and summation, respectively. Since h is the dominating factor in the formation of the structural non-idealities, there is negligible anisoelectricity when h is small, even if α is very large. Thus we restrict our analysis to cases of varying h and a small value of α ($\alpha = .01$ degrees). With this value for α , structural imperfections can be detected with a precision of .001 (the numerically acquired h/k_n = the theoretical $h/k_n \pm .001$) over the range of the theoretical h , making it suitable to detect anisoelectricity ranging from $100\% > |h/k_n| > 10\%$ with over 99% accuracy and $10\% > |h/k_n| > 1\%$ with over 90% accuracy. A fundamental lower limit is reached when $|h/k_n| = .1\%$ where the algorithm can no longer accurately detect errors (Figure 8).

4.3. Forced Dynamic Deflection

In this simulation, we implemented the feedback energy compensating controller from Equation (25) and re-ran the same case study as the previous section while letting Q be 30. This Q is based off Couette flow and squeeze film gas damping models¹ for the device in Figure 1. It was found that with a gain of less than .025 ($\gamma_2 < .025$), it was possible to accurately extract the structural non-idealities without the controller interfering with the measurement of anisoelectricities. Higher gains result in interference with the quadrature error, resulting in erroneous results. Without interference, the limits of the algorithm are the same as the un-forced dynamic case.

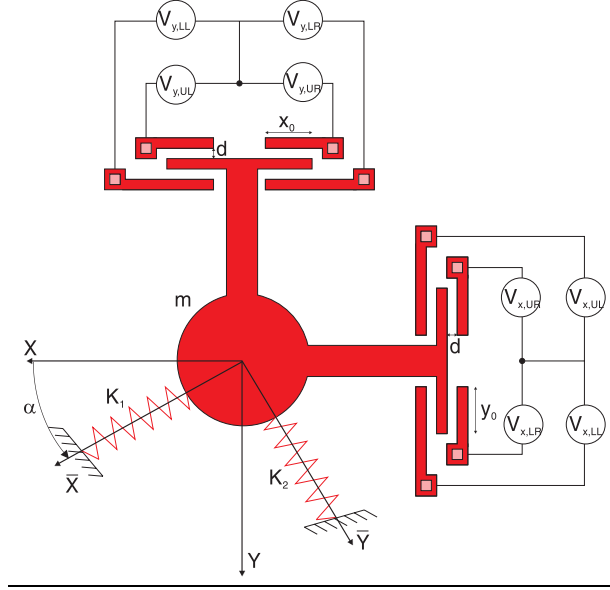


Figure 9. We use the inherent non-linearity of the parallel plate electrodes along the x and y direction in order to tune out the non-ideal stiffness elements.

5. IMPLEMENTATION

5.1. Electrostatic Tuning

Two different physical mechanisms were reported in MEMS for active frequency tuning, electrostatic trimming¹ and thermal tuning.¹¹ Since the angular gyroscope utilizes parallel plate electrodes for drive and sense, we focus on using the inherent non-linearity of the electrostatic forces to tune out the non-ideal components of the stiffness matrix (Figure 9). For the applied voltages, we use¹

$$\begin{aligned} V_{x,UL} &= V_{DC} - v_{xq} & V_{x,UR} &= V_{DC} + v_{xq} \\ V_{x,LL} &= V_{DC} + v_{xq} & V_{x,LR} &= V_{DC} - v_{xq} \\ V_{y,UL} &= V_{DC} - v_{yq} & V_{y,UR} &= V_{DC} + v_{yq} \\ V_{y,LL} &= V_{DC} + v_{yq} & V_{y,LR} &= V_{DC} - v_{yq} \end{aligned} \quad (27)$$

where V_{DC} is a constant bias voltage and v_{xq} and v_{yq} are quadrature control voltages. The nonlinearity of the parallel plate drives leads to a nonlinear electrostatic contribution to the overall system stiffness matrix. Combining the ideal, non-ideal, and electrostatic contributions together forms the total stiffness realization

$$\begin{aligned} K &= K_{ideal} + K_{nonideal} + K_{electrostatic} \\ K_{ideal} &= \begin{bmatrix} k_n & 0 \\ 0 & k_n \end{bmatrix} \\ K_{nonideal} &= \begin{bmatrix} h \cos(2\alpha) & h \sin(2\alpha) \\ h \sin(2\alpha) & -h \cos(2\alpha) \end{bmatrix} \\ K_{electrostatic} &= \frac{4\epsilon_0 t}{d^2} \begin{bmatrix} -\frac{g}{d} (V_{DC}^2 + v_{xq}^2) & (V_{DC} v_{xq} + V_{DC} v_{yq}) \\ (V_{DC} v_{xq} + V_{DC} v_{yq}) & -\frac{g}{d} (V_{DC}^2 + v_{yq}^2) \end{bmatrix} \end{aligned} \quad (28)$$

Here, t is the out-of-plane thickness and x_0 and y_0 are the electrode overlaps, which we have assumed to be equal ($x_0 = y_0 = g$). We have made a small deflection assumption such that the gap spacings $d - x$ and $d - y$ are approximately equal to d (see Figure 9). With an arbitrary DC voltage, we can find an appropriate set of control voltages to cancel the off-diagonal terms of the stiffness matrix and set the on-diagonal stiffness terms equal to each other (k_{tuned}).

$$v_{xq} = -\frac{1}{8} \frac{d (8 \cos(2\alpha) \epsilon_0 t V_{DC}^2 + g h \sin^2(2\alpha) d)}{g \sin(2\alpha) \epsilon_0 t V_{DC}} \quad (29)$$

$$v_{yq} = -\frac{1}{8} \frac{d (-8 \cos(2\alpha) \epsilon_0 t V_{DC}^2 + g h \sin^2(2\alpha) d)}{g \sin(2\alpha) \epsilon_0 t V_{DC}} \quad (30)$$

Because the electrostatic stiffness term is always negative, the tuned on-diagonal stiffness values will always be less than the original ideal stiffness ($k_{tuned} < k_n$).

6. CONCLUSION

In this paper, we have shown several algorithms for detection of structural anisoelectricities in a MEMS rate integrating gyroscope. We have shown that while an algorithm using static deflections is advantageous in its simplicity, it lacks the precision comparable to dynamic detection due to required knowledge of forces and precise deflections. The dynamic detection shows to be a more optimal method by using PCA and Fourier transforms, which take advantage of all the acquired data points. We have also shown that this algorithm can be used even in heavily damped systems by employing an energy compensating controller. The results of these detection schemes can be used in the feedforward stage of a dual-stage feedback/feedforward control architecture. As an example, we have shown the implementation of the feedback control using the nonlinear effects of electrostatic parallel plates.

7. ACKNOWLEDGEMENTS

The author would like to thank the Department of Defense who is sponsoring this work through a 2001 National Defense Science and Engineering Graduate Fellowship.

REFERENCES

1. W. A. Clark, *Micromachined Vibratory Rate Gyroscopes*. PhD thesis, UC Berkeley, 1997.
2. M. Putty, and K. Najafi, "A micromachined vibrating ring gyroscope," in *IEEE Solid State Sensors and Actuators Workshop*, pp. 213–220, Hilton Head Island, SC, June 1996.
3. A. Shkel and R. T. Howe, "Polysilicon Surface Micromachined Rate Integrating Gyroscopes." UC-Berkeley Office of Technology and Licensing. Case Number B99-077.
4. A. Shkel, "Smart MEMS: micro-structures with error-suppression and self-calibration control capabilities," in *The American Control Conference*, Arlington, CA, June 2001.
5. C. Painter and A. Shkel, "Structural and thermal modeling of a MEMS angular gyroscope," in *2001 SPIE Annual International Symposium on Smart Structures and Materials*, Newport Beach, CA, March 2001.
6. A. Shkel, R. Horowitz, A. Seshia, and R.T. Howe, "Dynamics and control of micromachined gyroscopes," in *The American Control Conference*, pp. 2119–2124, San Diego, CA, June 1999.
7. A. Shkel, R.T. Howe, and R. Horowitz, "Modeling and simulation of micromachined gyroscopes in the presence of imperfections," in *1999 International Conference on Modeling and Simulation of Microsystems*, pp. 605–608, San Juan, Puerto Rico, April 1999.
8. A. Basilevsky, *Statistical Factor Analysis for Related Methods, Theory and Applications*, John Wiley & Sons, Inc., 1994.
9. Young-Ho Cho, Byung Man Kwak, Albert P. Pisano, and Roger T. Howe, "Viscous energy dissipation in laterally oscillating planar microstructures: a theoretical and experimental study," in *IEEE Proceedings of Micro Electro Mechanical Systems Workshop*, Fort Lauderdale, FL, February 1993.
10. V. F. Zhuravlev, "Oscillation shape control in resonant systems," *J. Appl. Maths Mechs.* **56**(5), pp. 725–735, 1992.
11. T. Remtema and L. Lin, "Active Frequency Tuning for Microresonators by Localized Thermal Stressing Effects," in *Solid-State Sensor and Actuator Workshop*, pp. 363–366, Hilton Head Island, SC, June 2000.